DEFORMATION MONITORING USING
RADAR INTERFEROMETRY AND SENTINEL-1 DATA

Michele Crosetto[1], Oriol Monserrat[1], Núria Devanthéry[1], María Cuevas-González[1],
Anna Barra[1], Bruno Crippa[2] and Qihuan Huang[3]
[1]Centre Tecnològic de Telecomunicacions de Catalunya (CTTC), Division of Geomatics
Av. Gauss 7, E-08860, Castelldefels (Barcelona), Spain
Email: (mcrosetto, omonserrat, ndevanthery, mcuevas, abarra)@cttc.cat
[2]Department of Geophysics, University of Milan, Via Cicognara 8, I-20129, Milan, Italy
Email: bruno.crippa@unimi.it
[3]School of Earth Sciences and Engineering, Hohai University, PR China; E-Mail: insar@hhu.edu.cn

KEY WORDS: Radar, SAR, Differential Interferometry, Monitoring, Deformation.

ABSTRACT: This paper is focused on land deformation monitoring using remotely sensed, interferometric Synthetic Aperture Radar (SAR) data. The paper briefly describes three different techniques to perform the deformation monitoring. The first one is the standard Differential Interferometric Synthetic Aperture Radar (DInSAR) analysis, which is usually based on single pairs of SAR images. The second one is a simplified Persistent Scatterer Interferometry (PSI) approach, which is tailored to the characteristics of the Sentinel-1 data. The third one is a full PSI approach, which allows us getting an automatic control of the processing errors and of the quality of the derived deformation estimates. The paper shows DInSAR and PSI results coming from both the X-band TerraSAR-X and the C-band Sentinel-1 sensors. The results concern a co-seismic deformation field, an example of urban deformation monitoring, where multiple deformation phenomena occur, two examples of land deformation induced by underground water extraction, and an example of detection and monitoring of landslides.

1. INTRODUCTION

This paper is focused on land deformation monitoring using two complementary techniques: Differential Interferometric Synthetic Aperture Radar (DInSAR) and Persistent Scatterer Interferometry (PSI). The paper shows results coming from the X-band TerraSAR-X and from the C-band Sentinel-1 sensors.

The DInSAR technique represents the simplest way to exploit Synthetic Aperture Radar (SAR) imagery to measure and monitor land deformation. The technique requires at least a pair of SAR images acquired over the same area. For a review of DInSAR see Bamler and Hartl (1998) and Rosen et al. (2000). DInSAR has been widely exploited in the last three decades, yielding remarkable results in different fields, including:

- seismology (Massonnet et al., 1993; Peltzer and Rosen, 1995),
- vulcanology (Massonnet et al., 1995; Massonnet and Sigmundsson, 2000; Antonielli et al. 2014),
- glaciology (Goldstein et al., 1993; Rignot et al., 1997),
- landslides (Carnec et al., 1996; García-Davalillo et al., 2014),
- ground subsidence and uplift (Galloway et al., 1998; Amelung et al., 1999), etc.

Comprehensive reviews of DInSAR applications are provided by Massonnet and Feigl (1998) and Hanssen (2001).

The PSI technique represents an advanced class of the DInSAR techniques, which makes use of multiple SAR images acquired over the same site and appropriate tools to separate the deformation signal of interest from other components of the PSI observations, like the residual topographic error component, the atmospheric component and the phase noise. For a comprehensive review of PSI, including its applications, refer to Crosetto et al. (2016).

The DInSAR and PSI techniques have experienced a major development in the last decades, which has been mainly related to the progress accomplished through the exploitation of C-band data from ERS-1/2, Envisat and Radarsat sensors. The data acquired by these satellites cover long periods of time, which is a key aspect to guarantee a long-term deformation monitoring. The advent of very high resolution X-band data, in 2007 with the sensors TerraSAR-X and CosmoSkyMed, enabled a major step forward in the PSI techniques, e.g. see Crosetto et al. (2010). A new significant improvement is occurring thanks to the data acquired by the C-band sensors on board the Sentinel-1A and 1B satellites.

2. DESCRIPTION OF THE TECHNIQUES

This section briefly summarizes the DInSAR and PSI techniques used by the authors to derive the results described in the following section. They include a standard DInSAR analysis, a simplified PSI approach and a full PSI approach.

The standard DInSAR analysis is usually based on single pairs of SAR images. This simple analysis can be useful to study fast deformation phenomena, e.g. see Biescas et al (2007), or to measure displacements occurred in a short period of time when compared to the satellite revisiting time, e.g. co-seismic deformation. The best results are achieved using several pairs of interferograms and restricting the analysis to small areas, see Crosetto et al. (2002).

A simplified PSI approach is used to exploit two key characteristics of the Sentinel-1 data. The first one is the increased interferometric coherence, which is mainly due to the short revisiting cycle of these data (6 days using both the Sentinel-1A and 1B data). The approach exploits temporally consecutive interferograms. The second aspect is the reduced orbital tube of Sentinel-1, which decreases the importance of the so-called residual topographic error (RTE) (Crosetto et al., 2016). In this approach, this phase component is neglected. The main steps of the procedure are briefly outlined below. (i) Given a stack of N complex SAR images, generate the N-1 consecutive multi-look interferograms. (ii) Perform a 2D phase unwrapping of the N-1 interferograms. (iii) Directly integrate the interferometric phases, to obtain temporally ordered phases in correspondence to the image acquisition dates. The phase of the first image is usually set to zero. (iv) Estimation of the atmospheric phase screen (APS) component and its removal. This is performed by means of a set of spatio-temporal filters. (v) The deformation time series are derived by removing the atmospheric phase component and transforming the phases into displacements. (vi) The final step is data geocoding. Some examples of results derived with the simplified PSI approach are shown in the next section.

The full PSI approach requires a redundant set of M interferograms, where M is much greater than N. The main steps are briefly described below. (i) Given a stack of N complex SAR images, generate M redundant multi-look interferograms. (ii) Perform the so-called 2+1D phase unwrapping. This involves a spatial 2D phase unwrapping and a 1D phase unwrapping, which is performed pixel wise over the M interferograms. This last step is able to detect and correct the errors generated during the 2D phase unwrapping stage, and provides tools to control the quality of the derived time series (Devanthéry et al., 2014). It uses an iterative least squares procedure, which fully exploits the integer nature of the unwrapping errors. (iii) Estimation of the atmospheric component and its removal. (iv) Deformation velocity and RTE estimation. The deformation velocity and RTE are computed over a set of PSs, from the M wrapped atmosphere-free interferograms, using the method of the periodogram. This step can be performed using multi-look interferograms, or full-resolution interferograms. (v) RTE removal. The RTE phase component is removed from the wrapped APS-free interferograms. The linear deformation component can optionally be removed and then, in a later stage, added back to the deformation time series. (vi) Perform the final iteration of the 2+1D phase unwrapping. This involves a 2D phase unwrapping, followed by a 1D phase unwrapping. In this stage are generated the final deformation time series. (vii) The final step is data geocoding. This approach allows us to get an automatic control of the unwrapping errors and of the quality of the derived deformation estimates. In addition, it properly takes into account the RTE component of the PSI observations (this is neglected in the simplified approach). The major drawback with respect to the simplified approach is the reduced spatial sampling that can be achieved. Some examples derived using the full PSI approach are shown below.

3. EXAMPLES OF DEFORMATION MONITORING RESULTS

This section illustrates some examples of deformation monitoring results derived with the three techniques described in the previous section, using TerraSAR-X (X-band) and Sentinel-1 (C-band) data.

3.1 Co-seismic deformation: Menyuan 2016 earthquake

The example is based on a standard DInSAR analysis. It concerns the co-seismic deformation field associated with the 6.4-magnitude Menyuan earthquake occurred on 21 January 2016 in the Qinghai province, China. The analysis was based on an ascending (images from 13/1/16 to 6/2/16) and a descending (images from 18/1/16 to 11/2/16) interferograms derived with Sentinel-1A images (Figure 1). The two co-seismic field patterns are rather similar, besides the different geometric distortions of these interferograms caused by the topography of this high mountain area. The maximum line-of-sight co-seismic deformation for both interferograms is approximately 6.75 cm: we can therefore deduce that the observed deformation is mainly vertical. This case study shows the importance of the S-1 background data acquisition, which is essential to obtain the pre- and post-seismic images required to estimate co-seismic deformation fields in remote areas. The co-seismic field can be used to estimate the main characteristics of the earthquake at hand.
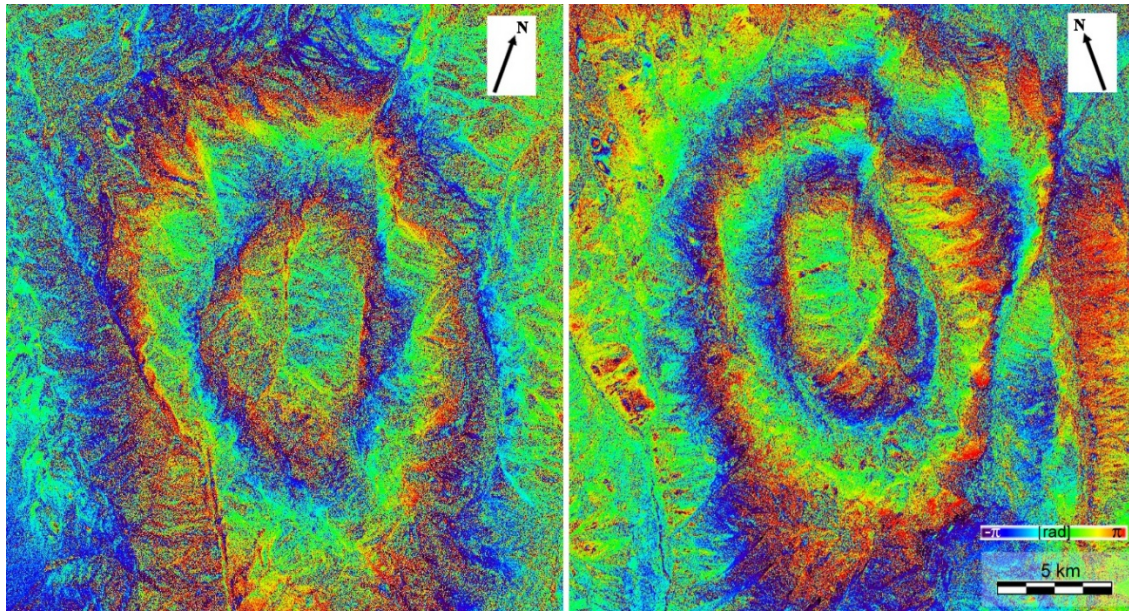
Figure 1. Ascending (left) and descending (right) wrapped interferograms displaying the co-seismic deformation field of the Menyuan earthquake (China) occurred on 21 January 2016 (Beijing Time).
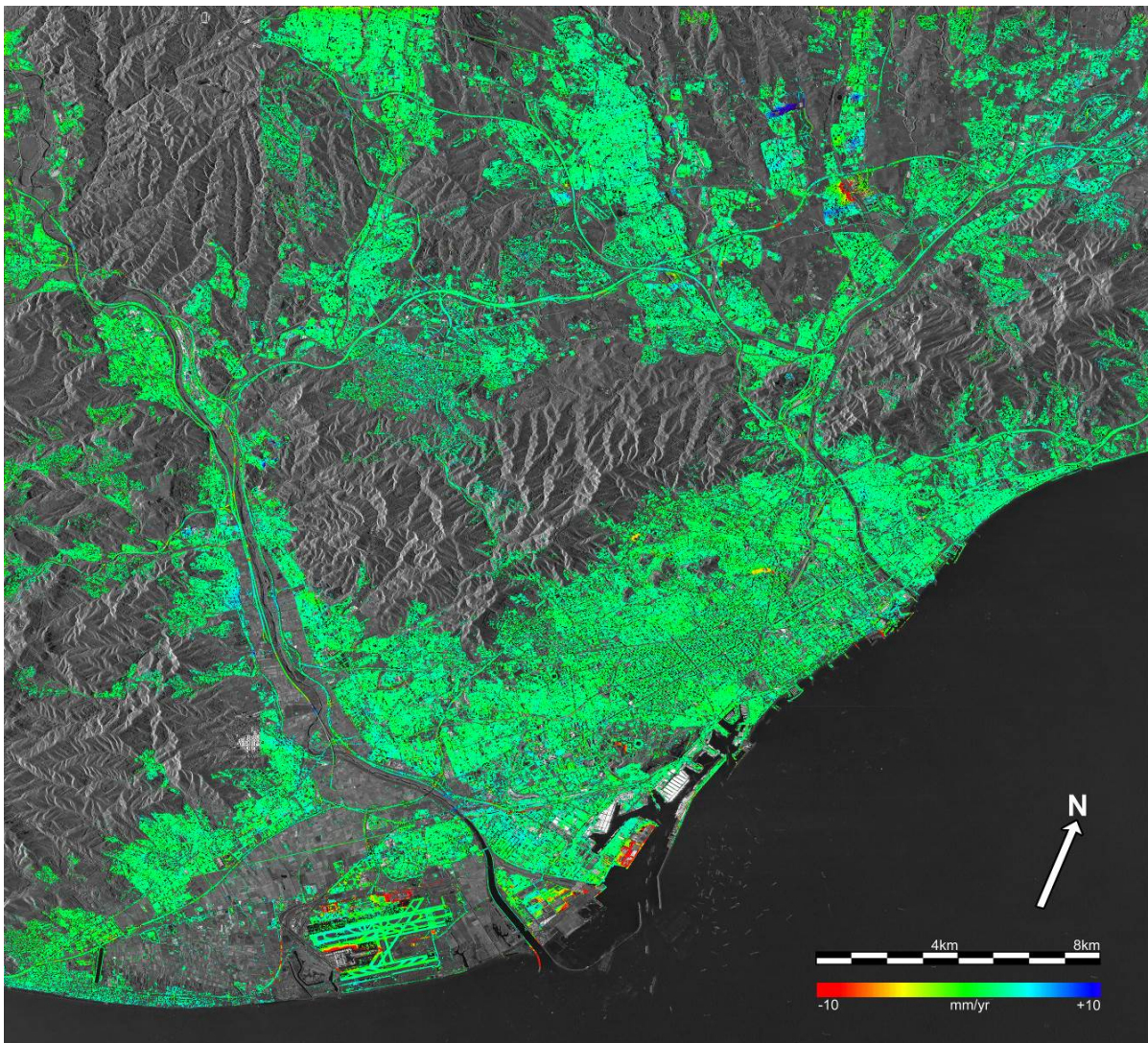

Figure 2. Deformation velocity map over Barcelona superposed to a mean SAR amplitude image. The map covers 1019 km^2. It was derived using 28 TerraSAR-X images from December 2007 to November 2009.

3.2 Urban deformation monitoring: Barcelona

This example is based on an advanced PSI approach, using 28 X-band TerraSAR-X data that cover the metropolitan area of Barcelona (Spain). These images span the period from December 2007 to November 2009. The deformation velocity map of the full TerraSAR-X frame is shown in Figure 2. 5.4 million PSs were measured oven an area of 1019 km^2. Only the major deformation phenomena are visible in Figure 2, e.g. the airport and the port of Barcelona and other subsidence and uplift areas located at the top right part of the image. However, hundreds of deformation phenomena of different size and magnitude were found. There are several examples of deformation caused by soil compaction, water abstraction (see Section 3.3), landslides, underground construction works (metro line and metro stations), etc. These results represent a valuable source of information for public and private entities in charge of the maintenance of indispensable assets of the Barcelona metropolitan area.
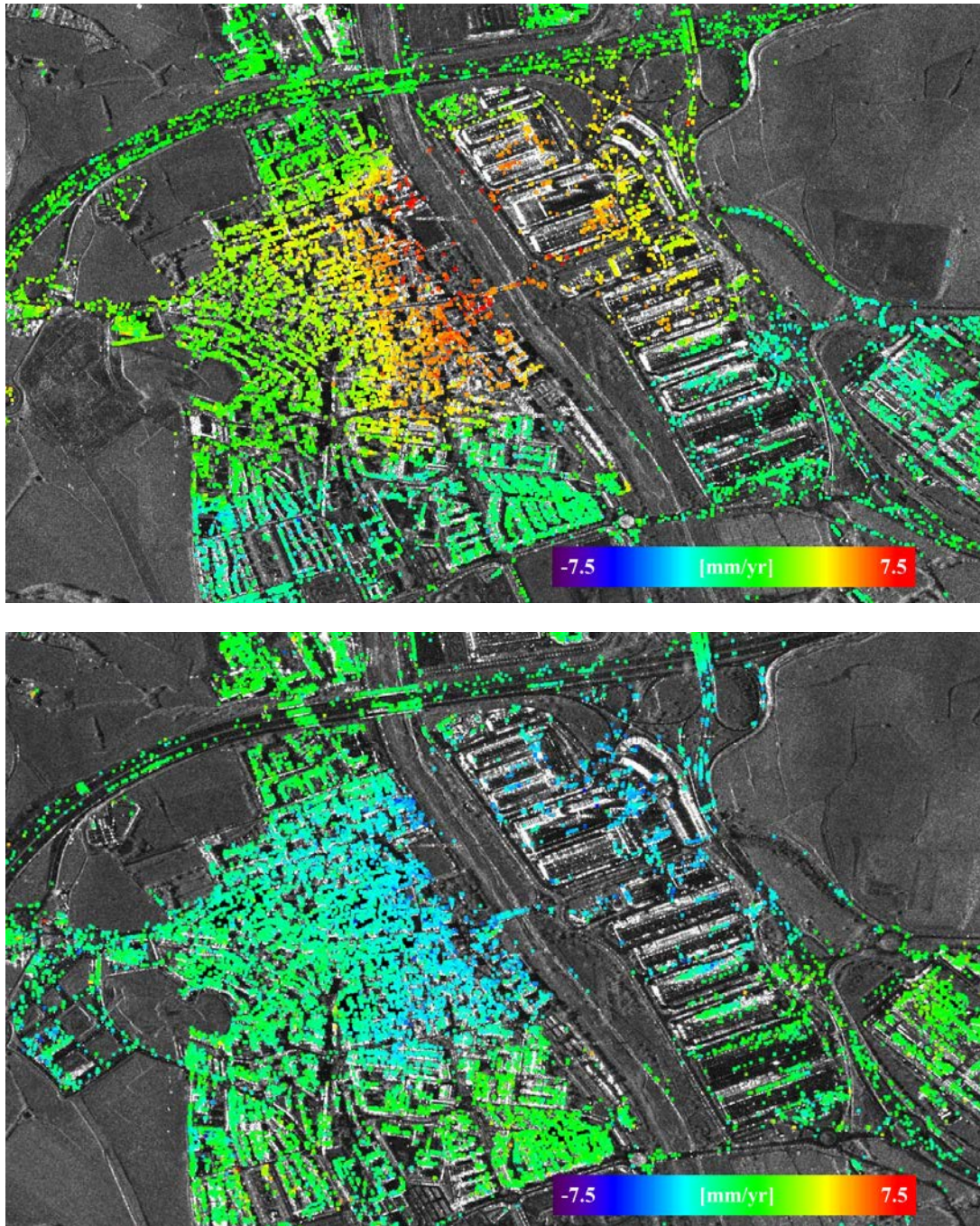

Figure 3. Deformation velocity maps over a small city of the metropolitan area of Barcelona derived using TerraSAR-X images. The map above corresponds to a period from 2007 to 2012, while the map below covers the period 2013-2014. The velocity maps are superposed to a mean SAR amplitude image.

3.3 Deformation due to water extraction: example from the Barcelona area

An interesting application of PSI is the monitoring of the land deformation induced by the extraction of underground water, which represents a valuable (and sometime scarce) natural resource. The example illustrated in Figure 3 concerns a small city of the metropolitan area of Barcelona. It was derived using X-band TerraSAR-X images and an advanced PSI approach. Two periods were analysed: 2007-2012 and 2013-2014. In the first period (Figure 3, above) a subsidence is measured, which interests a large part of the area of interest. The maximum deformation rates are up to 7.5 mm/yr. Interestingly, during the second observed period the same area is subjected to an uplift, which interests the same area previously subsiding. In this case the uplift rates are up to 3 mm/yr. From these results we can deduce that a strong water extraction activity was going on during the period 2007-2012, while the extraction was stopped during the period 2013-2014, originating a partial recovery of the previous deformation.

3.4 Deformation due to water extraction: Mexico DF

This example encompasses a significant portion of Mexico DF. It was derived using Sentinel-1A images and an advanced PSI approach. The processed area covers approximately 80 by 25 km. A density of 575 Persistent Scatterers per square kilometre has been achieved, measuring a total of 720882 points. Figure 4 shows a deformation map derived from 10 Sentinel-1 images and a total of 45 interferograms. Positive values (blue) indicate displacements towards the SAR, while the negative ones (red) denote displacements away from the SAR sensor. The map shows a large area affected by subsidence (red) with displacement values of up to 9 cm occurred during the four months of observations.

3.5 Landslide detection and monitoring: Molise (Italy)

This result was derived using the simplified PSI approach. It comes from a project to detect and monitor landslides in the Molise region (Southern Italy), see for details Barra et al. (2016). The analysis was based on 14 Sentinel-1A ascending images acquired in the period from October 2014 to April 2015. Figure 5 shows a map of the total accumulated deformation in the observed 6 months. Most of the accumulated deformation values have values close to zero, which correspond to the green colours. Two sets of landslides are visible in this area. Their approximate borders are indicated by red contours. In the upper part of the image, the landslides are characterized by blue colours: as indicated by the red arrow, the landslide displacement is toward the sensor (the images were taken from ascending orbits). The maximum line-of-sight displacements of these landslides are up to 13 cm. In the lower part of the figure, there is another set of landslides, which in this case are characterized by red colours. Their displacement is away from the sensor. The maximum line-of-sight displacements of these landslides are up to 12 cm.

Figure 5 represents an example of positive PSI result. The key factor is surely a high coherence over the entire stack of processed interferograms, see the coherence of the interferogram shown in the lower-right part of Figure 5. With high coherence values the phase unwrapping is usually reliable, with phase unwrapping errors confined to local non-coherent areas. By contrast, the procedure becomes cumbersome in presence of very low coherence area, where the phase unwrapping tends to systematically fail.
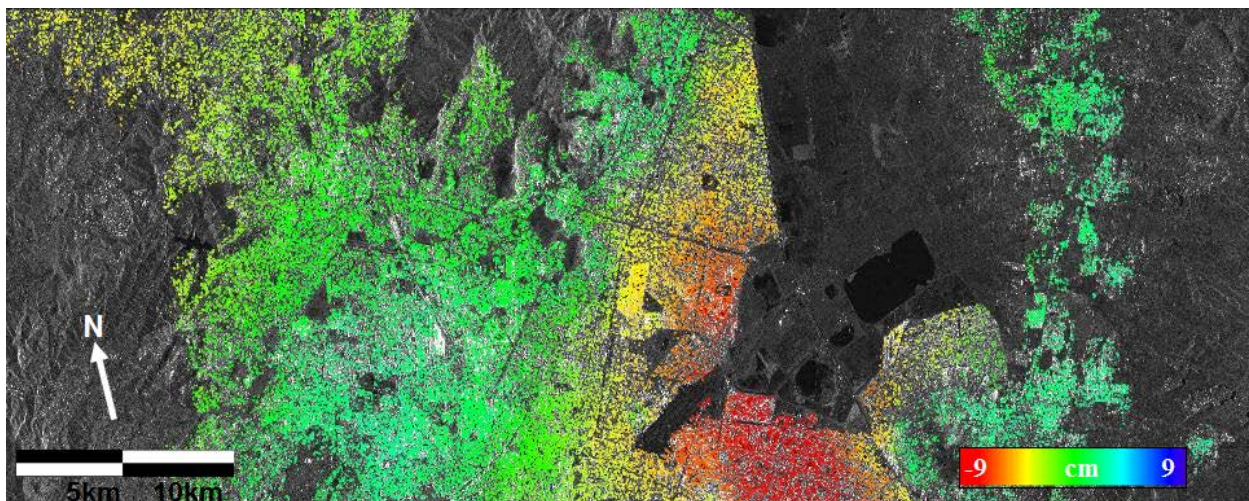

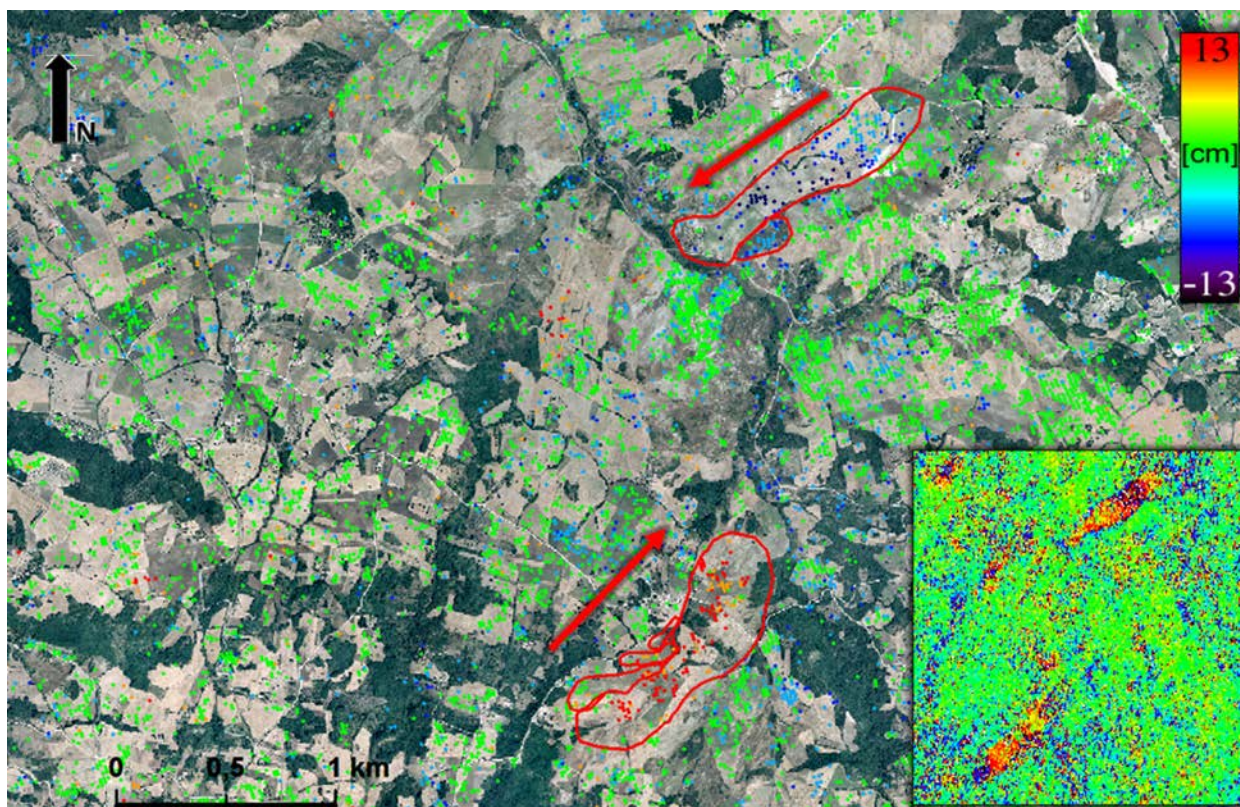Figure 4. Accumulated deformation map over the area of Mexico DF.

Figure 5. Landslides detected using the simplified PSI approach: accumulated deformation map observed over a period of approximately 6 months in the Molise region (Southern Italy). 12-day wrapped interferogram of the same area, where the landslides are visible (lower-right).

4. ACKNOWLEDGEMENTS

5. REFERENCES

Amelung, F., Galloway, D.L., Bell, J.W., Zebker, H.A., Laczniak, R.J., 1999. Sensing the ups and downs of Las Vegas: InSAR reveals structural control of land subsidence and aquifer-system deformation. Geology, 27(6), pp. 483-486.

Antonielli, B., Monserrat, O., Bonini, M., Righini, G., Sani, F., Luzi, G., Feyzullayev, A.A., Aliyev, C.S., 2014. Pre-eruptive ground deformation of Azerbaijan mud volcanoes detected through satellite radar interferometry (DInSAR). Tectonophysics, 637, pp. 163-177.

Bamler, R., Hartl, P., 1998. Synthetic aperture radar interferometry. Inverse Probl, 14, R1-R54.

Barra, A., Monserrat, O., Mazzanti, P. Esposito, C., Crosetto, M., Scarascia Mugnozza, G., 2015. First insights on the potential of Sentinel- 1 for landslides detection. Geomatics Natural Hazards and Risks. Vol 7, Issue 6, pp. 1-10.

Biescas, E.; Crosetto, M.; Agudo, M.; Monserrat, O.; Crippa, B, 2007. Two radar interferometric approaches to monitor slow and fast land deformations. J. of Surveying Engineering 2007, 133 (2), pp. 66-71.

Carnec, C., Massonnet, D., King, C., 1996. Two examples of the use of SAR interferometry on displacement fields of small spatial extent. Geophysical Research Letters, 23(24), pp. 3579-3582.

Crosetto, M.; Tscherning, C.C.; Crippa, B.; Castillo, M., 2002. Subsidence Monitoring using SAR interferometry: reduction of the atmospheric effects using stochastic filtering. Geophysical Research Letters, 29 (9), pp. 26-29.

Crosetto, M., Monserrat, O., Iglesias, R., Crippa, B., 2010. Persistent Scatterer Interferometry: potential, limits and initial C- and X-band comparison". Photogrammetric Engineering & Remote Sensing, 76(9), pp. 1061-1069.

Crosetto, M., Monserrat, O., Cuevas-González, M., Devanthéry, N., Crippa B., 2016. Persistent Scatterer Interferometry: a review. ISPRS Journal of Photogrammetry and Remote Sensing, 115, pp. 78-89.

Devanthéry, N., Crosetto, M., Monserrat, O., Cuevas-González, M., Crippa, B., 2014. An Approach to Persistent

Scatterer Interferometry. Remote Sensing, 6(7), pp. 6662-6679.

Galloway, D.L., Hudnut, K.W., Ingebritsen, S.E., Phillips, S.P., Peltzer, G., Rogez, F., Rosen, P.A., 1998. Detection of aquifer system compaction and land subsidence using interferometric synthetic aperture radar, Antelope Valley, Mojave Desert, California. Water Resources Research, 34(10), pp. 2573-2585.

García-Davalillo, J.C., Herrera, G., Notti, D., Strozzi, T., Álvarez-Fernández, I., 2014. DInSAR analysis of ALOS PALSAR images for the assessment of very slow landslides: the Tena Valley case study. Landslides, 11(2), pp. 225-246.

Goldstein, R.M., Engelhardt, H., Kamb, B., Frolich, R.M., 1993. Satellite radar interferometry for monitoring ice sheet motion: application to an Antarctic ice stream. Science, 262(5139), pp. 1525-1530.

Hanssen, R., 2001. Radar interferometry. Kluwer Academic Publishers, Dordrecht (The Netherlands).

Massonnet, D., Rossi, M., Carmona, C., Adragna, F., Peltzer, G., Feigl, K., Rabaute, T., 1993. The displacement field of the Landers earthquake mapped by radar interferometry. Nature, 364(6433), pp. 138-142.

Massonnet, D., Briole, P., Arnaud, A., 1995. Deflation of Mount Etna monitored by spaceborne radar interferometry. Nature, 375, pp. 567-570.

Massonnet, D., Feigl, K.L., 1998. Radar interferometry and its application to changes in the Earth's surface. Reviews of geophysics, 36(4), pp. 441-500.

Massonnet, D., Sigmundsson, F., 2000. Remote sensing of volcano deformation by radar interferometry from various satellites. In: Mouginis-Mark et al. (eds), Remote sensing of active volcanism. Geophysical monograph, 116, pp. 207-221.

Peltzer, G., Rosen, P., 1995. Surface displacement of the 17 May 1993 Eureka Valley, California, earthquake observed by SAR interferometry. Science, 268(5215), pp. 1333-1336.

Rignot, E.J., Gogineni, S.P., Krabill, W.B., Ekholm, S., 1997. North and northeast Greenland ice discharge from satellite radar interferometry. Science, 276(5314), pp. 934-937.

Rosen, P.A., Hensley, S., Joughin, I.R., Li, F.K., Madsen, S.N., Rodriguez, E., Goldstein, R.M., 2000. Synthetic aperture radar interferometry. Proceedings of the IEEE, 88(3), pp. 333-382.